Spontaneous imbibition in coal with in-situ dynamic micro-CT imaging

Yuejian Lu[a, b], Dameng Liu [a,b]*, Yidong Cai [a,b], Qian Li[a, b], Yingfang Zhou[c]

[a]*School of Energy Resources, China University of Geosciences, Beijing 100083, China*

[b]*Coal Reservoir Laboratory of National Engineering Research Center of CBM Development & Utilization, China University of Geosciences, Beijing 100083, China*

[c]*School of Engineering, Fraser Noble Building, King's College, University of Aberdeen, AB24 3UE Aberdeen, UK*

Abstract

The gas/fluid flowing behavior and fluid distribution under capillary forces in porous media are essential for evaluating the pore-fracture characteristics of coal. Capillary force is crucial for flow-back efficiency after hydraulic fracturing during enhanced coalbed methane (CBM) production. In this work, in situ dynamic X-ray micro-computed tomography (X-ray μ-CT), field emission scanning electron microscopy (FE-SEM) combined with mercury intrusion porosimetry (MIP) were used on two coal samples of different wettability to explore the behavior of spontaneous imbibition. The results show that both pore-fracture and mineral content could affect the imbibition behavior of coal, which the former has played a major role. The spontaneous imbibition process can be divided into 4 stages to reveal fluid flow characteristics by the fluid distribution at different time steps. The gas relative permeability of coal attenuates exponentially with imbibition time result for capillary force based on fractal theory (the gas relative permeability reduces its value from 0.72 mD to 0.01 mD for WD, 0.5 mD to 0.08 mD for WZX). A low flow-back rate of fracturing fluid would lead to severe permeability damage. The longer the return drainage time, the more severe the

permeability damage.

Keyword: coalbed methane; spontaneous imbibition; x-ray; relative permeability

1. Introduction

Coalbed methane (CBM), an unconventional resource, has raised considerable concerns as its benefit for safe mining, friendly environmental effect, and significant economic value over last few decades (Cai et al., 2018; Vishal et al., 2015; Zhou et al., 2018; Roslin et al., 2020). CBM reservoirs in China normally characterized as low permeability, low porosity, and high in-situ stress due to their complex geothermal dynamics and buried depth (Gbadamosi et al., 2018; Zhai et al., 2015). There are few opportunities to improve CBM production with general stimulation techniques used in conventional reservoir, such as carbon dioxide sequestration technology, chemical methods and hydraulic fracturing technology (Ibrahim & Nasr-El-Din, 2017), however, with hydraulic fracturing is currently the most popular technology to improve the permeability of unconventional reservoirs (Jiang et al., 2016; Yin et al., 2018; Zhou et al., 2016). Flow-back is an essential step after hydraulic fracturing to avoid the migration channel being occupied by fracturing fluid. However, the effective flow rate generally is lower than 30%, there is a quantity of hydraulic fluid staying in the pore-fractures after hydraulic fracturing due to the capillary force, which would result dramatic CBM production decline during the drainage (Engineer, 1985; Holditch, 1979; King, 2012; Tannich, 1975; Yang et al., 2017).

During the flow-back process, fracturing liquid will be imbibed into pore-fractures of the CBM reservoir, which would affect the pressure release, desorption, diffusion, and permeability of methane (Cai et al., 2014; Shen et al., 2018a; Roslin et al., 2019). Spontaneous imbibition will result in permeability damage in general (Shen et al., 2016; Zhou et al.,2016), especially in CBM reservoirs with plenty of nano-pores with strong capillary force (Shen et al., 2018a). Water molecules would replace the sorption sites for methane due to its stronger adsorption capacity (Levy et al., 1997; Švábová et al., 2011; Wang et al., 2018). Previous research suggested that if the pressure difference between inside and outside of pore is smaller than the capillary entry pressure, the diffusion pathway would be blocked by fracturing fluid, and thus resulting in water locking effect and reduce methane diffusivity in coal matrix (Busch and Gensterblum, 2011; Chareonsuppanimit et al., 2014); they also claimed that the water saturation of coal have a positive relationship with water permeability and have a positive relationship with start-up pressure gradient. However, component sorption/desorption measurements indicated that water in coal matrix would improve CBM production, especially for high-rank coal (Busch et al., 2003); this was also explained in some re-opened well if the capillary force is driving force for CBM production (Habibi et al., 2015; Shen et al., 2016). Spontaneous imbibition widely exists in various oil/gas reservoirs; however, its mechanism is still obscure and needs to be explored.

Spontaneous imbibition refers to non-wetting fluids being replaced by wetting fluid under capillary and gravity force (Cai et al., 2012; Meng et al., 2019; Morrow and Mason, 2001; Schmid et al., 2016; Yuan et al., 2019; Zhang et al., 1996). The process of spontaneous imbibition is complex, and mainly constrained by pore characterization, wettability, initial water saturation of reservoir, mineral composition, and fluid property

(Cai et al., 2020; Dehghanpour et al., 2013; Gao and Hu, 2016, 2018; Ma et al., 1999; Makhanov et al., 2012; Mason et al., 2010). Typically, spontaneous imbibition volume and fluid flow behavior can be acquired with multiple techniques, including nuclear magnetic resonance, neutron imaging technology, scanning electron microscopy, and numerical simulation (DiStefano et al., 2017; Gao and Hu, 2018; Jafari et al., 2017; Yuan et al., 2019). However, very limited research has been focused on visualizing and quantifying the process of imbibition and fluid distribution in coals.

In this work, potassium iodide solution (KI, 10% weight) was used as imbibition liquid to visualize the process of fluid imbibition for coal plugs during X-ray μ-CT imaging. First, water imbibition, fractures, and minerals were segmented and interpreted with Avizo 9.0. Then imbibition water flow characteristics and the controlling factors of imbibition were discussed. Finally, we investigated the effect of imbibition on gas-water relative permeability based on fractal theory.

2. Materials and Methods

2.1 Coal sampling and analyses

Two coal samples were collected from Wudong coal mine in Junggar Basin and Wangzhuang coal mine in Qinshui Basin, respectively. All samples were sent to the experimental lab for coal basic analysis, mercury intrusion porosimetry, and X-ray μ-CT. The maximum vitrinite reflectance (Ro, max) was measured in the Beijing Key Laboratory of Unconventional Natural Gas Geology Evaluation and Development Engineering, China University of Geosciences (CUGB), following the Chinese National Standard ISO 7404.3-1994 (Zhou et al., 2017). Cylindrical cores with the diameters of ~2.5 cm and length of ~5.0 cm was obtained parallel to the bedding from each coal block. These cores were used in the X-ray μ-CT and MIP.

2.2 Mercury Intrusion Porosimetry

Mercury Intrusion Porosimetry (MIP) experiment is widely used to obtain pore structure, pore size distribution and pore connectively of rock due to its convenient and fast, which could acquire wider pore size range compared to N_2 adsorption/desorption experiment (Yang et al.,2020). Two coal plugs with 2.5cm in diameter were collected for MIP experiment by using the PoreMasterGT60 (Quantachrome, US) based on the Chinese Oil and Gas Industry Standard of SY/T 5346-2005(Yao et al., 2012). The measurement capillary pressure was increase to 200.6 MPa to assure as small as 4 nm pore size could be detected. The mercury intrusion/extrusion curves could be obtained based on capillary pressure and mercury saturation in coal, and pore diameter and pore size distribution could be calculated from the curves. Analysis results from MIP were required as shown in section 3.1.

2.3 Contact angle measurement

Contact angle measurement is widely used to characterize the wettability between solid and liquid (Ibrahim & Nasr-El-Din, 2016). We first cut the larger coal sample into 1cm ×1cm×1cm, and then the coal surface was polished with 30-grit, 600-grit and 1500-grit sandpapers, respectively, the coal surface was coated with 0.5 μm alumina powders (Gao et al., 2020). Contact angles of two coal samples were measured using the sessile drop method with contact angle meter (JC2000D) in CUGB at 25°C and 0.1MPa, the results of wettability for coal samples as shown in Fig.1.

2. 4 In-situ dynamic X-ray μ-CT

Before commencing X-ray μ-CT scanning measurements, two coal plugs with 25mm in diameter and 50mm in height were oven-dried at 105°C for 24h to remove the immobile water in the coal sample. In order to reduce the influence of water evaporation during the spontaneous imbibition, the side of coal plugs was coated with heat-shrinkable film. In situ dynamic X-ray μ-CT experiment was performed using a Nano Voxel-3000 X-ray 3-D microscope in spiral scanning mode at the Institute of Mechanics, Chinese Academy of Sciences (CAS) at 25℃ and 0.1MPa. Spiral scanning mode allows improving scanning speed while keeping a high resolution of the image (Wang et al., 2018). The X-ray μ-CT scanning configuration condition was as following: voxel size of the sample, 14.46 μm; the number of pixels:1920×1920; tube voltage, 170 kV. For each coal sample CT scanning session, a total of 3630 and 4647 scan images were obtained for sample WD and sample WZX, respectively.

It is noted that all slices must be aligned for different spontaneous imbibition steps of the CT scanning experiment. Thus, the sample needs to be remained in the same position and its state of rest during the measurement. The coal plug was fixed with an acrylic plastic tube, as shown in Fig.2, which could solve the problem above because of its low density (1.0128–1.0621 g/cm3) and low CT number (Hirono et al., 2003). Spontaneous imbibition liquid (potassium iodide solution, 10% weight) (Klise et al., 2016) was then transferred with pipettor to control continuous imbibition that occurs or not.

Before spontaneous imbibition, X-ray μ-CT measurement at dry condition was firstly carried out to require the base information of CT intensity. Subsequently, imbibition liquid was injected into the acrylic plastic tube to fill up to the bottom surface of the coal plug (co-current imbibition). The imbibition fluid was removed after 15 minutes of spontaneous imbibition and prepare for CT scanning. Finally, repeating the above steps completes two samples under the same condition for 60 min, 120 min, 240 min, 600 min, and 1440 min successively.

2. 5 Image processing

Fig. 3 shows 520th CT slice images of the WD samples required by x-ray μ-CT, as well as the minerals, fractures and imbibition fluid in the coal segmented by the different methods. Before analyzing the sample X-ray μ-CT experimental data, the noise produced in the imaging should be removed with a median filtering method to improve the signal to noise ratio (SNR) (Li et al., 2020), and components in coal could be segmented more accurately. After X-ray μ-CT scanning in dry condition, the original CT signal of samples could be obtained (Fig.3a); thus, pores, fractures, and minerals could be analyzed. The exact segmentation of the main components in coal was one of the key steps in this paper; local thresholding method and Top-Hat segmentation method can identify fractures, minerals, coal matrix, and imbibition water based on the different CT intensity value of research object. Local thresholding method distinguish two substances with setting a critical CT intensity value, which could identify imbibition water clearly in this work (Fig.3f), specific steps are the same as shown in our previous work (Li et al., 2017). There lies in the fact that fractures and minerals developed in a certain direction in coal (Yao et al., 2009), single local thresholding method would not segment above components integrally, and may influence the accuracy of experimental data. Based on the characteristic of fractures and minerals in slice images, combine Top-Hat segmentation method with region growing method could distinguish fractures and minerals accurately with the margin of experiment error (Fig.3d, Fig.3e) (Zhu et al., 2019). Top-Hat segmentation method has a significant advantage in extracting small elements and details from given 2D slice images and could detect extremely low CT intensity or extremely high-intensity, which requests regular edge details (fractures and minerals) and large background (coal matrix in this work) in the slice image as shown in Fig.3g, Fig.3h (Chen et al., 2002). One type of Top-Hat segmentation is Black Top-Hat, which was used to detect fractures in this study, and another type (White Top-Hat) was used to detected mineral.

Mineral percentage and imbibition water saturation of coal samples are defined as:

$$P_m\%=\frac{N_{mineral}}{N_{total}}\times 100\% \tag{1}$$

$$S_w\%=\frac{N_{water}}{N_{total}}\times 100\% \tag{2}$$

Where $P_m\%$ and $S_w\%$ are mineral content and imbibition water saturation, respectively; $N_{mineral}$ and N_{water} are mineral Voxel count and imbibition water Voxel count, N_{total} is total voxel count of the slice.

Avizo 9.0.1 software was adopted for 3D reconstruction in this work. Due to the large size of original 3-D reconstruction data (1920×1920×3620 for sampled WD and 1920×1920×4647 for sample WZX), the image was cropped into 600×600×2350 of sample WD and 600×600×3400 of sample WZX for subsequent analysis.

2. 6 Gas/water relative permeability

Gas relative permeability and water relative permeability could be calculated based on fractal geometry theory (Zhang et al., 2017). Fractal dimension was obtained with mercury porosimetry experiment, which can be expressed as:

$$N(>r) = \int_{r}^{r_{max}} P(r)dr = ar^{-D} \quad (3)$$

Where r is pore diameter, $N(>r)$ is the counts of pores with a diameter larger than r, r_{max} is the maximum pore diameter in the coal, $P(r)$ is the pore size distribution function, a is a constant, D is the fractal dimension, which is between 2 and 3 for pore-fractures(Mikula.et.al, 1987)

$$P(r) = \frac{dN(>r)}{dr} = a'r^{-D-1} \quad (4)$$

According to Eq. (4), the accumulation pore volume of pores with diameter less than r, $V(<r)$, and total pore volume, $V(total)$, could be represented as:

$$V(<r) = \int_{r_{\min}}^{r} P(r)\alpha r^3 dr = a''(r^{3-D} - r_{\min}^{3-D}) \quad (5)$$

$$V(total) = \int_{r_{\min}}^{r_{\max}} P(r)\alpha r^3 dr = a''(r_{\max}^{3-D} - r_{\min}^{3-D}) \quad (6)$$

Where α is a constant related to pore structure, and $a'' = a'\alpha/(3-D)$.

Thus, the saturation of pore with less than r from Eq. (5) and Eq. (6) could be calculated as:

$$S = \frac{V(<r)}{V} = \frac{a''(r^{3-D}-r_{\min}^{3-D})}{a''(r_{\max}^{3-D}-r_{\min}^{3-D})} = \frac{r^{3-D}-r_{min}^{3-D}}{r_{max}^{3-D}-r_{min}^{3-D}} = (\frac{r}{r_{max}})^{3-D} \quad (7)$$

$$P_c = \frac{2\sigma\cos\theta}{r} \quad (8)$$

Where P_c is capillary pressure, σ is the surface tension of a liquid, θ is contact angle.

Combining the Eq. (7) and Eq. (8):

$$S = (\frac{P_c}{P_{min}})^{D-3} \quad (9)$$

According to the works of the previous scholar (Burdine.et.al., 1953; Purcell.et.al., 1949), relative permeability can be expressed as following based on fractal theory:

$$k_{rg} = S'^{\frac{11-3D}{3-D}} \quad (10)$$

$$k_{rw} = (1 - S')^2 (1 - S'^{\frac{5-D}{3-D}}) \quad (11)$$

Where k_{rg} is gas relative permeability, k_{rw} is water relative permeability, S' is effective wetting phase saturation, which is imbibition water saturation in this work

3. Results

3.1 Mercury intrusion porosimetry

The properties of the coal samples were summarized in Table 1, as shown in this table, long-flame coal for sample WD (R_o = 0.68) and meager coal for sample WZX (R_o = 2.05) were collected. The mercury intrusion/extrusion curves and pore size distribution of two coal sample with MIP are presented in Fig.4, in this figure, sample WD and WZX have similar mercury intrusion/extrusion curves shape with three stages, including straight-line stage, platform stage, and smooth curve stage, there lies in the fact that pore structure in two coal samples is similar. Based on Eq. (8), the mercury injection process represents that seepage-pores (>100 nm) are well developed in two coals, the pores with diameter less than 10 nm in WD is more developed than WZX (Fig.4b, Fig.4e). Pore fractal dimension D could be calculated with 3-K based on fractal theory in section gas/water relative permeability, where K is the slope of fitting line in Fig.4c and Fig.4f, and the fractal dimension is 2.71 and 2.6 for sample WD and WZX, respectively, that is, pore in WD is more complex than WZX, which might be related to the development of pore in coal.

3.2 Water distribution in coal during spontaneous imbibition

Fig.5 shows water distribution and saturation curve of coal sample in vertical direction in WD sample at different times under spontaneous imbibition conditions calculated from CT scan.

As shown in figure, air in pore- fracture system was replaced by imbibition water due to the capillary force form 0 h to 24 h. The longer the imbibition time correspond the higher the imbibition water, which increase to 29.23% of coal plug after imbibition for 15 minutes (Fig.5a) and raise to the 57.42% of the plug at 1 hour (Fig.5b). Subsequently, according to the imbibition CT image in Fig.5e, the imbibition water reached the top of the coal plug before 10 hours; however, this does not mean the imbibition effect to a halt; the spontaneous imbibition saturation slightly increased from 6.82% at 10 hours to 7.76% at 24 h as shown in Table 2.

Moreover, a few detailed observations on the imbibition water behavior could be found based on a close examination of images in Fig.5. At the initial imbibition stage (Fig.5a and Fig.5b), water was imbibed into pore networks of coal matrix rather than fractures, and fractures are not imbibition channels distinguished by the naked eye as shown P area in Fig.5g. For the later part of spontaneous imbibition, as imbibition saturation continue to increase, the scale and connectivity of fractures may become a critical factor in maintaining the imbibition activity flowing. Water was imbibed into fractures indicates their water-wet property, which is consistent with contact angle experiments (CA_water =15°, as shown in Fig.1). However, we found some fractures could not be saturated with water (n and m area in Fig.5h) after 24h of water imbibition, this means that different wettability (mixed wet) for coal at the micro-scale.

3.3 Water imbibition capability

Spontaneous imbibition involves two main stages including rapid rise stage and smooth curve stage as presented in spontaneous imbibition saturation curves of Fig.6. At the very beginning of imbibition, hydrostatic pressure could be ignored due to the small volume of water, and thus the capillary force is the only force that acts on the water. The square of imbibition mass is linear to the imbibition time, as revealed by previous research (Li et al., 2016). The imbibition process can be governed by Eq. (12) (Handy, 1960), which is consistent with experimental measurements on the imbibition water distribution of μ-CT.

$$Q_w^2 = (\frac{2P_c k_w \varphi A^2 S_w}{\mu_w})t \tag{12}$$

Here Q_w equals the total volume of water imbibed, P_c and k_w are capillary force and permeability respectively, A is the cross-sectional area of the sample, μ_w is water viscosity, φ is porosity, t is imbibition time.

The imbibition curve was divided into three sections based on the gradient of spontaneous imbibition saturation curves as shown in Fig.6, which were in good agreement with the main imbibition pathway obtained from μ-CT images at different imbibition stages as presented in Fig.7. The first one is the capillary zone dominated by capillary forces, and water was mainly imbibed into pores (Fig.7a), in this part, gravity can be ignored due to little water imbibition in coal, pores in coal matrix is main imbibition pathway. Capillary force is weaker and the gravity is stronger compared with capillary zone, and water imbibition rate is obviously declined in second part, which is also called transition zone. Pores and micro-fractures in coal are main imbibition pathway (Fig.7b). With respect to the last part, (Shen et al., 2016) considered that water imbibition diffuse to the deeper coal matrix, and mainly controlled by chemiosmosis, however, this is not inconsistent with our experiment with fractures are main imbibition pathway (Fig.7c). Spontaneous imbibition stage and a corresponding main imbibition pathway of WD and WZX shown in Table 3.

We noted there are different imbibition saturation curves between the two samples. For sample WD, a total of capillary zone and transfer zone last for an extended period of 600 min; however, the time is 120 min for sample WZX (see Fig.6). This phenomenon is mainly because of poor-developed, fractures are the main channels for imbibition, which indicates a single imbibition path for sample WZX, and water could be imbibed into coal in a short time in the early stage of imbibition. Moreover, part of pores filled with minerals are the important factor of low porosity as shown in Fig.8, which lead final imbibition water saturation being far below that of the sample WD.

4. Discussion

4.1 Effect of fracture development on SI

Generally speaking, the permeability of coal is mainly contributed by fractures compared with coal matrix (Yao et al., 2020); thus, exploring the relationship between fractures and imbibition behavior could provide a basis for the optimization of favorable areas in CBM reservoirs. Previous scholars have studied the effect of pore type and structure on imbibition (Shen et al., 2018b); however, the impact of fractures in coal on imbibition has rarely been studied.

In this work, fracture porosity of XY-slice were analyzed by the same method as in previous research (Cai et al., 2014). Meanwhile, the proportion of imbibition at different time in these slices was calculated by Eq. (5), the relationship between fracture porosity and the ratio of imbibition as presented in Fig.9. The proportion of imbibition shows a negative linear correlation as fracture porosity increases after spontaneous imbibition for 15 min, which indicates that fractures are not conducive to water flow in coal (Fig.9a). While the proportion of imbibition has a positive correlation with fracture porosity at time of1, 2, 4, 10, and 24 h (Fig.9b-f), which indicates fractures play an increasingly important part in spontaneous imbibition during the later period of imbibition. Pores in coal were saturated by imbibition water in the late-stage of imbibition; fractures become dominant pathways of imbibition (Fig.7c). The wall of fracture would form thin water film because of disjoining pressure under the long-distance van der Waals adhesion force (Derjaguin and Churaev, 1974), as show in Fig.10. Thin water film on the fracture surface would increase the wettability of fractures and thereby increase the capillary pressure based on Eq. (3). On the other hand, the formation of thin water film would decrease the diameter of the fracture (see stage IV in Fig.11,), which could also increase the water imbibition volume.

4.2 Fluid flow behavior in fracture of coal

To better compare the dynamic imbibition behavior and spatial distribution at different times, we analyzed the scale of imbibition water with Avizo software. Fractures were classified into three types according to the length to facilitate better explore their distribution features: fracture A (1 μm < length ≤ 3.5 mm), fracture B (3.5 mm < length ≤ 6.5 mm), fracture C (6.5 mm < length ≤ 10 mm). Fig.12a1-a6 show water in different scale fractures by spontaneous imbibition for 15 min, 1h, 2h, 4h, 10h, 24h, respectively. With the increase of spontaneous imbibition time, the distribution of water in fractures is inconsistent and displays remarkable migration characteristics. The imbibition water is mainly distributed in the micro-fractures less than 4 mm at 15 minutes, as shown in

Fig.12a1. However, we also found the existence of imbibed fluid in the fractures above 8mm, which shows apparent with our previous analysis in section 4.1.1 that large fractures played a dominant role in the late stage of imbibition. This is mainly because the large fractures located at the bottom of the coal plug are in contact with the imbibition liquid and could be saturated with water by capillary force.

A comparison of the curves at a different time in Fig 10a reveals the spatial distribution of the imbibed water in coal. From Fig.12b-f we can investigate that the difference between the two curves (Fig.12b, Fig.12c, Fig.12d, Fig.12e, Fig.12f) is the result of water migration. The imbibition process shows a phase difference; water was imbibed into fracture A and fracture B at the primary stage ranging from 15 min to 1 h as shown in Fig.12b. At this imbibition stage, gas (CH_4 in coal reservoir) adsorption sites in micropores would be replaced by water molecules due to the weaker solid-gas interaction(Crosdale et al., 2008; Jin and Firoozabadi, 2014), with high moisture content resulting in elevated gas desorption during this imbibition period. Almost no fluid flows out from the fracture, but water was imbibed into more extensive fractures increasingly in the next hour (see Fig.12c). The water in fracture B followed by escaping quickly; at the same time, some water was continue imbibed into fracture A and fracture B (Fig.12d). For the next 6 hours (4h-10h), the status of water flow and distribution become more complicated, in fracture B and fracture C, and there are not only fluid inflow but also fluid outflow (Fig.12e), fluid in different fractures developed countercurrent imbibition effects during this period and could improve the recovery of CBM(Takahashi and Kovscek, 2010). For the last 14 hours (10h-24h) period (Fig.12f), a significant quantity of liquid migrates to fracture C from fracture A, forming an aggregation effect of fluid. this may due to the clay mineral on the wall of fractures react with water changed surface properties and resulted in higher interfacial tension(Peng and Xiao, 2017). the schematic of four stages during spontaneous imbibition is shown in Fig.11.

4.3 Effect of mineral content on SI.

Fig.8 shows the pore-fracture characteristics and development of mineral are different for samples WD and WZX. The sample WZX was suitable to investigate the relationship between mineral component and imbibition water due to its undeveloped pore-fracture networks and abundant mineral. The statistical approach of mineral content in different CT slices is the same as presented in the section 4.1. Imbibition volume in coal correlates well with the mineral content; more water would be imbibed with the increase of mineral content during the whole imbibition period as shown in Fig.13. Moreover, mineral content and imbibition volume became increasingly correlated as the increase of imbibition time with a correlation coefficient is 0.5701 at 15 min rise to 0.8707 at 24 hours (Table.4), which is the same as a previous study with various methods(Gao and Hu, 2016; Yang et al., 2018).

Combined with the X-ray fluorescence (XRF) and SEM, the factors influencing the imbibition volume included intercrystalline pore in clay minerals and water sensitivity of clay minerals (Fig.8). Capillary force is dominated by pore size based on Eq. (5). Nano-pores in the mineral of coal could provide enough capillary force and a storage place for imbibition water during the imbibition process, which could not be detected with the N_2 adsorption method (Yang et al., 2019). Besides, the hydrophilic nature of clay mineral also plays an important role in imbibition (Bertoncello et al., 2014). Water-wet porosity of clay could provide more adsorption sites than in coal matrix for the water molecule, the more content of clay minerals, the more water would be imbibed. Moreover, clay swelling would create more micro-fractures leading higher imbibition volume due to the hydration during spontaneous imbibition (Zolfaghari et al., 2017). Although both fracture porosity and mineral content have a positive correlation with water imbibe ition volume after 15 min of imbibition, and the imbibition ability of sample WD is stronger than sample WZX, that is, the effect of minerals on imbibition is less than pore-fractures.

4.4 Gas-water relative permeability change during spontaneous imbibition.

It is found that CBM flowing rate are controlled by gas and water content in the fracture of coal reservoir, and the flow capacity of each type fluid in the fracture will be disturbed by other fluids (Shen et al., 2020). In addition, understanding gas-water relative permeability is important to evaluate the productivity of CBM during the drainage, including design of fracturing technology, estimations of CBM productivity, and optimizations of CBM well operations (Chen et al., 2013).

The slope of fitting line between lg(r) and lg(S) is 0.29 and 0.4 for WD and WZX, respectively (Fig.4c and Fig.4f). Thus, the fractal dimension calculation is 2.71 and 2.6 by mercury intrusion porosimetry experimental data (section 3.1) and Eq. (7), gas-water relative permeability curves of two samples, as shown in Fig.14a-b. The equal-permeability point is crucial to evaluating coal wettability, the higher water saturation that corresponds to the equal-permeability point, the more hydrophilic of coal sample(Chang et al., 1997). The results of fractal theory show sample WD has a stronger water-wet than sample WZX with equal-permeability saturation is 76.5% and 70.8%, respectively, as shown in Fig.13a and Fig.13b.

The data from the X-ray μ-CT experiment is applied into Eq. (10) and Eq. (11); the change of gas-water permeability could be calculated during the whole spontaneous imbibition, as presented in Fig.14c-d. The gas relative permeability of coal attenuates exponentially with imbibition time result for capillary force. This result reveal that the low flow-back rate of fracturing fluid would lead to severe permeability damage; the longer of flow-back is, the permeability damage would be severer. Moreover, the permeability damage rate (the gas relative permeability reduces its value from 0.72 mD to 0.01 mD for WD, 0.5 mD to 0.08 mD for WZX) would increase with the wettability (Fig.14c and Fig.14d). Thus, shortening flow-back time is necessary as to enhance the CBM recovery with hydraulic fracturing technique.

5. Conclusions

Visualizing dynamics of flowing water was used to investigate the spontaneous imbibition behavior and its controlling factors in CBM reservoirs. Imbibition water distribution, fracture porosity, and mineral content of each XY-slice of coal plug were acquired to illustrate imbibition behavior and the effect of fractures and minerals on imbibition. The gas-water permeability during the whole spontaneous imbibition was calculated by using fractal theory and in-situ X-ray μ-CT experiment in combination. This work could provide insights into the understanding of the complicated imbibition process and will be favorable for improving the efficiency of hydraulic fracturing.

Conclusions are made as follows:

1) Coal sample from Wudong has stronger water imbibition capacity than WZX sample because of its developed pore-fracture and more hydrophilic. Water imbibition volume were positively associated with fracture porosity during the process of imbibition, except at the primary stage of imbibition. In addition, more water would be imbibed with the increase of mineral content during the whole imbibition period, which maybe results from intercrystalline pore in clay minerals and water sensitivity of clay minerals.
2) Imbibition process could be divided into four stages: Stage I, water was imbibed into pores and micro-fractures; Stage II, water was imbibed into lager fracture with length more than 3.5 mm; Stage III, imbibition water exchange between micro-fractures and macro-fractures frequently; Stage IV, some imbibition water flow into macro-fractures from micro-fractures, forming some thin water film on the surface of the macro-fractures.
3) Gas flowing rate are controlled by water content in the fracture of coal reservoir. Results show the gas relative permeability of coal attenuates exponentially with imbibition time based on fractal theory, which reduces its value from 0.72 mD to 0.01 mD for WD, 0.5 mD to 0.08 mD for WZX, low flow-back rate of fracturing fluid would lead severe permeability damage, the longer flow-back is, the severer permeability damage would be. While guaranteeing fracturing effect, shortening flow-back time is necessary after hydraulic fracturing.

Acknowledgements

This research was funded by the National Natural Science Fund (Grant No. 41830427, 41772160 and 41922016) and the Fundamental Research Funds for Central Universities (Grant No. 2652019254). The authors declare that they have no known competing financial interests or personal relationships that could have appeared to influence the work reported in this paper.

Nomenclature:

P_m% = Mineral content, -
S_w% = Imbibition water saturation, -
r = Pore diameter, m;
r_{max} = The maximum pore diameter, m;
$N(> r)$ = Counts of pores with a diameter larger than r, -;
D = Fractal dimension, -;
α = Constant related to pore structure, -;
σ = Surface tension of liquid, N/m;
P_c = Capillary pressure, MPa;
θ = Contact angle, °;
k_{rg} = Gas relative permeability, -;
k_{rw} = Water relative permeability, -;
S' = Effective wetting phase saturation,

References

Bertoncello, A., Wallace, J., Blyton, C., Honarpour, M., and Kabir, C. S. 2014. Imbibition and water blockage in unconventional reservoirs: well management implications during flowback and early production. In SPE/EAGE European unconventional resources conference and exhibition (Vol. 2014, pp. 1–13). European Association of Geoscientists and Engineers. https://doi.org/10.2118/167698-MS.

Burdine, N. 1953. Relative permeability calculations from pore size distribution data. J PETROL TECHNOL 5(03), 71–78. https://doi.org/10.2118/225-G.

Busch, A., and Gensterblum, Y. 2011. International Journal of Coal Geology Review article CBM and CO2-ECBM related sorption processes in coal : A review. Int J Coal Geol 87(2), 49–71. https://doi.org/10.1016/j.coal.2011.04.011.

Busch, A., Gensterblum, Y., and Krooss, B. M. 2003. Methane and CO_2 sorption and desorption measurements on dry Argonne premium coals: pure components and mixtures. Int J Coal Geol, 55, 205–224. https://doi.org/10.1016/S0166-5162(03)00113-7.

Cai, J.C., Hu, X.Y., Standnes, D. C., and You, L.Y. 2012. An analytical model for spontaneous imbibition in fractal porous media including gravity. COLLOID SURFACE A 414, 228–233. https://doi.org/10.1016/j.colsurfa.2012.08.047.

Cai, J.C., Perfect, E., Cheng, C.-L., and Hu, X.Y. 2014. Generalized Modeling of Spontaneous Imbibition Based on Hagen–Poiseuille Flow in Tortuous Capillaries with Variably Shaped Apertures. LANGMUIR 30(18), 5142–5151. https://doi.org/10.1021/la5007204.

Cai, J.C., Li, C.X., Song, K.P., Zou, S.M., Yang, Z.M., Shen, Y.H., Meng,Q.B., and Liu,Y. 2020. The influence of salinity and mineral components on spontaneous imbibition in tight sandstone. Fuel 117087. https://doi.org/10.1016/j.fuel.2020.117087.

Cai, Y.D., Liu, D.M., Mathews, J. P., Pan, Z.J., Elsworth, D., Yao, Y.B.,Li,J.Q., and Guo,X.Q. 2014. Permeability evolution in fractured coal—Combining triaxial confinement with X-ray computed tomography, acoustic emission and ultrasonic techniques. Int J Coal Geol 122, 91–104. https://doi.org/10.1016/j.coal.2013.12.012.

Cai, Y.D., Li, Q., Liu, D.M., Zhou, Y.F., and Lv, D.W.2018. Insights into matrix compressibility of coals by mercury intrusion porosimetry and N_2 adsorption. Int J Coal Geol 200(October), 199–212. https://doi.org/10.1016/j.coal.2018.11.007.

Chang, Y. C., Mohanty, K. K., Huang, D. D., and Honarpour, M. M. 1997. The impact of wettability and core-scale heterogeneities on relative permeability. J Petrol Sci Eng 18(1), 1–19. https://doi.org/10.1016/S0920-4105(97)00006-5.

Chareonsuppanimit, P., Mohammad, S. A., Robinson, R. L., and Gasem, K. A. M. 2014. Modeling gas-adsorption-induced swelling and permeability changes in coals. Int J Coal Geol 121, 98–109. https://doi.org/10.1016/j.coal.2013.11.009.

Chen, D., Pan, Z.J., Liu, J.S., and Connell, L. D. 2013. An improved relative permeability model for coal reservoirs. Int J Coal Geol 109–110, 45–57. https://doi.org/10.1016/j.coal.2013.02.002.

Chen, T., Wu, Q. H., Rahmani-Torkaman, R., and Hughes, J. 2002. A pseudo top-hat mathematical morphological approach to edge detection in dark regions. Pattern Recogn 35(1), 199–210. https://doi.org/10.1016/S0031-3203(01)00024-3.

Crosdale, P. J., Moore, T. A., and Mares, T. E. 2008. Influence of moisture content and temperature on methane adsorption isotherm analysis for coals from a low-rank, biogenically-sourced gas reservoir. Int J Coal Geol 76(1–2), 166–174. https://doi.org/10.1016/j.coal.2008.04.004.

Dehghanpour, H., Lan, Q., Saeed, Y., Fei, H., and Qi, Z. 2013. Spontaneous imbibition of brine and oil in gas shales: Effect of water adsorption and resulting microfractures. Energ Fuel 27(6), 3039–3049. https://doi.org/10.1021/ef4002814.

Derjaguin, B. V, and Churaev, N. V. 1974. Structural component of disjoining pressure. J Colloid Interf Sci 49(2), 249–255. https://doi.org/10.1016/0021-9797(74)90358-0.

DiStefano, V. H., Cheshire, M. C., McFarlane, J., Kolbus, L. M., Hale, R. E., Perfect, E., et al. 2017. Spontaneous imbibition of water and determination of effective contact angles in the Eagle Ford Shale Formation using neutron imaging. J Earth Sci-China 28(5), 874–887. https://doi.org/10.1007/s12583-017-0801-1.

Engineer, R. 1985. Cal Canal Field, California: Case History of a Tight and Abnormally Pressured Gas Condensate Reservoir. SPE California Regional Meeting. Bakersfield, California: Society of Petroleum Engineers. https://doi.org/10.2118/13650-MS.

Friesen, W. I., and Mikula, R. J. 1987. Fractal dimensions of coal particles. J Colloid Interf Sci 120(1), 263–271. https://doi.org/10.1016/0021-9797(87)90348-1.

Gao, Y.S., Jung, S.H, & Pan, L. 2020. Interaction and instability of air films between bituminous coal surfaces and surfactant droplets. Fuel, 274, 117839. ttps://doi.org/10.1016/j.fuel.2020.117839

Gao, Z.Y., and Hu, Q.H. 2016. Initial water saturation and imbibition fluid affect spontaneous imbibition into Barnett shale samples. J Nat Gas Sci Eng 34, 541–551. https://doi.org/10.1016/j.jngse.2016.07.038.

Gao, Z.Y., and Hu, Q.H. 2018. Pore structure and spontaneous imbibition characteristics of marine and continental shales in China. AAPG Bull, 102(10), 1941–1961. https://doi.org/10.1306/03291817297.

Gbadamosi, A. O., Junin, R., Manan, M. A., Yekeen, N., Agi, A., and Oseh, J. O. 2018. Recent advances and prospects in polymeric nanofluids application for enhanced oil recovery. J Ind Eng Chem 66, 1–19. https://doi.org/10.1016/j.jiec.2018.05.020.

Habibi, A., Xu, M., Dehghanpour, H., Bryan, D., and Uswak, G. 2015. Understanding Rock-Fluid interactions in the montney tight oil play. In SPE/CSUR unconventional resources conference. SPE https://doi.org/10.2118/175924-MS.

Handy, L. L. 1960. Determination of effective capillary pressures for porous media from imbibition data. SPE 219(01), 75–80. https://doi.org/10.2118/1361-G.

Hirono, T., Takahashi, M., and Nakashima, S. 2003. In situ visualization of fluid flow image within deformed rock by X-ray CT. Eng Geol 70(1), 37–46. https://doi.org/10.1016/S0013-7952(03)00074-7.

Holditch, S. A. 1979. Factors affecting water clocking and gas flow from hydraulically fractured gas wells. J Pet Technol 31(12), 1515–1524.

https://doi.org/10.2118/7561-PA.

Jafari, I., Masihi, M., and Nasiri Zarandi, M. 2017. Numerical simulation of counter-current spontaneous imbibition in water-wet fractured porous media: Influences of water injection velocity, fracture aperture, and grains geometry. Phys Fluids 29(11), 113305. https://doi.org/10.1063/1.4999999.

Jiang, T.T., Zhang, J.H., and Wu, H. 2016. Experimental and numerical study on hydraulic fracture propagation in coalbed methane reservoir. J Nat Gas Sci Eng 35, 455–467. https://doi.org/10.1016/j.jngse.2016.08.077.

Jin, Z.H., and Firoozabadi, A. 2014. Effect of water on methane and carbon dioxide sorption in clay minerals by Monte Carlo simulations. Fluid Phase Equilibr 382, 10–20. https://doi.org/10.1016/j.fluid.2014.07.035.

King, G. E. 2012. Hydraulic fracturing 101: What every representative, environmentalist, regulator, reporter, investor, university researcher, neighbor and engineer should know about estimating frac risk and improving frac performance in unconventional gas and oil wells. SPE. https://doi.org/10.2118/152596-ms.

Klise, K. A., Moriarty, D., Yoon, H., and Karpyn, Z. 2016. Automated contact angle estimation for three-dimensional X-ray microtomography data. Adv Water Resour 95, 152–160. https://doi.org/10.1016/j.advwatres.2015.11.006.

Ibrahim, A. F., & Nasr-El-Din, H. A.2017. Effects of formation-water salinity, formation pressure, gas composition, and gas-flow rate on carbon dioxide sequestration in coal formations. SPE, 22(05), 1-530. https://doi.org/10.2118/185949-PA

Ibrahim, A. F., & Nasr-El-Din, H. A. 2016. Effect of water salinity on coal wettability during CO2 sequestration in coal seams. Energy & Fuels, 30(9), 7532-7542. https://doi.org/10.1021/acs.energyfuels.6b01205.

Levy, J. H., Day, S. J., and Killingley, J. S. 1997. Methane capacities of Bowen Basin coals related to coal properties. Fuel 76(9), 813–819. https://doi.org/10.1016/S0016-2361(97)00078-1.

Li, C.X., Shen, Y.G., Ge, H.K., Su, S., and Yang, Z.H. 2016. Analysis of spontaneous imbibition in fractal tree-like network system. Fractals 24(03), 1650035. https://doi.org/10.1142/S0218348X16500353.

Li, Q., Liu, D.M., Cai, Y.D., Zhao, B., Qiu, Y.K., and Zhou, Y.F. 2020. Scale-span pore structure heterogeneity of high volatile bituminous coal and anthracite by FIB-SEM and X-ray μ-CT. J Nat Gas Sci Eng 81, 103443. https://doi.org/10.1016/j.jngse.2020.103443.

Li, Z.T., Liu, D.M., Cai, Y.D., Ranjith, P. G., and Yao, Y.B. 2017. Multi-scale quantitative characterization of 3-D pore-fracture networks in bituminous and anthracite coals using FIB-SEM tomography and X-ray μ-CT. Fuel 209, 43–53. https://doi.org/10.1016/j.fuel.2017.07.088.

Ma, S. M., Zhang, X., Morrow, N. R., and Zhou, X. 1999. Characterization of wettability from spontaneous imbibition measurements. J Can Petrol Technol 38(13). https://doi.org/10.2118/99-13-49.

Makhanov, K., Dehghanpour, H., and Kuru, E. 2012. An experimental study of spontaneous imbibition in Horn River shales. SPE Canadian unconventional resources conference. SPE, https://doi.org/10.2118/162650-MS.

Mason, G., Fischer, H., Morrow, N. R., and Ruth, D. W. 2010. Correlation for the effect of fluid viscosities on counter-current spontaneous imbibition. J Petrol Sci Eng 72(1–2), 195–205. https://doi.org/10.1016/j.petrol.2010.03.017.

Meng, Q.B., Cai, Z.X., Cai, J.C, and Yang, F. 2019. Oil recovery by spontaneous imbibition from partially water-covered matrix blocks with different boundary conditions. J Petrol Sci Eng 172, 454–464. https://doi.org/10.1016/j.petrol.2018.09.075.

Morrow, N. R., and Mason, G. 2001. Recovery of oil by spontaneous imbibition. Curr Opin Colloid In. https://doi.org/10.1016/S1359-0294(01)00100-5.

Peng, S., and Xiao, X.H. 2017. Investigation of multiphase fluid imbibition in shale through synchrotron-based dynamic micro-CT imaging. JGR: Solid Earth 122(6), 4475–4491. https://doi.org/10.1002/2017JB014253.

Purcell, W. R. 1949. Capillary pressures-their measurement using mercury and the calculation of permeability therefrom. J Petrol Technol 1(02), 39–48. https://doi.org/10.2118/949039-G.

Roslin, A., Pokrajac, D., and Zhou, Y. 2019. Cleat structure analysis and permeability simulation of coal samples based on micro-computed tomography (micro-CT) and scan electron microscopy (SEM) technology. Fuel 254(May), 115579. https://doi.org/10.1016/j.fuel.2019.05.162.

Roslin, A., Pokrajac, D., Wu, K., and Zhou, Y. 2020. 3D pore system reconstruction using nano-scale 2D SEM images and pore size distribution analysis for intermediate rank coal matrix. Fuel 275(July 2019), 117934. https://doi.org/10.1016/j.fuel.2020.117934.

Schmid, K. S., Alyafei, N., Geiger, S., and Blunt, M. J. 2016. Analytical solutions for spontaneous imbibition: fractional-flow theory and experimental analysis. SPE Journal 21(06), 2–308. https://doi.org/10.2118/184393-PA.

Shen, J., Zhao, J.C., Qin, Y., Shen, Y.L., and Wang, G. 2018a. Water imbibition and drainage of high rank coals in Qinshui Basin, China. Fuel 211(August 2017), 48–59. https://doi.org/10.1016/j.fuel.2017.09.039.

Shen, J., Qin, Y., Li, YP., and Wang, G. 2020. Experimental investigation into the relative permeability of gas and water in low-rank coal, J Petrol Sci Eng 175, 303-316.https://doi.org/10.1016/j.petrol.2018.12.041.

Shen, Y.H., Ge, H.K., Li, C.X., Yang, X.Y., Ren, K., Yang, Z.H., and Su, S. 2016. Water imbibition of shale and its potential influence on shale gas recovery—a comparative study of marine and continental shale formations. J Nat Gas Sci Eng 35, 1121–1128. https://doi.org/10.1016/j.jngse.2016.09.053.

Švábová, M., Weishauptová, Z., and Přibyl, O. 2011. Water vapour adsorption on coal. Fuel 90(5), 1892–1899. https://doi.org/10.1016/j.fuel.2011.01.005.

Takahashi, S., and Kovscek, A. R. 2010. Spontaneous countercurrent imbibition and forced displacement characteristics of low-permeability, siliceous shale rocks. J Petrol Sci Eng, 71(1–2), 47–55. https://doi.org/10.1016/j.petrol.2010.01.003.

Tannich, J. D. 1975. Liquid Removal from Hydraulically Fractured Gas Wells. J Petrol Technol 27(11), 1309–1317. https://doi.org/10.2118/5113-PA.

Vishal, V., Singh, T. N., and Ranjith, P. G. 201). Influence of sorption time in CO2-ECBM process in Indian coals using coupled numerical simulation. Fuel, 139, 51–58. https://doi.org/10.1016/j.fuel.2014.08.009.

Wang, J.M., Qin, Q., Guo, L.L., and Feng, Y. 2018. Multi-fractal characteristics of three-dimensional distribution of reconstructed soil pores at opencast coal-mine dump based on high-precision CT scanning. Soil Till Res 182, 144–152. https://doi.org/10.1016/j.still.2018.05.013.

Wang, L., Wan, J.M., Tokunaga, T. K., Kim, Y., and Yu, Q.C. 2018. Experimental and Modeling Study of Methane Adsorption onto Partially Saturated Shales. Water Resour Res 54(7), 5017–5029. https://doi.org/10.1029/2017WR020826.

Yang, L., Ge, H.K, Shi, X., Li, J., Zhou, T., Cao, W.K, et al. 2017. Experimental and numerical study on the relationship between water imbibition and salt ion diffusion in fractured shale reservoirs. J Nat Gas Sci Eng 38, 283-297. https://doi.org/10.1016/j.jngse.2016.12.010.

Yang, L., Dou, N.H., Lu, X.B., Zhang, X.H., Chen, X., Gao, J., et al. 2018. Advances in understanding imbibition characteristics of shale using an NMR technique: a comparative study of marine and continental shale. J Geophys Eng 15(4), 1363–1375. https://doi.org/10.1088/1742-2140/aaaf76.

Yang, R., Hu, Q.H, Yi, J.Z, Zhang, B.Q, He, S., Guo, X.W., et al. 2019. The effects of mineral composition, TOC content and pore structure on spontaneous imbibition in Lower Jurassic Dongyuemiao shale reservoirs. Mar Petrol Geol 109, 268–278. https://doi.org/10.1016/j.marpetgeo.2019.06.003.

Yang, S.G., Yu, Q.C. 2020. Experimental investigation on the movability of water in shale nanopores: A case study of Carboniferous shale from the Qaidam Basin, China. Water Resources Res 56(8), e2019WR026973. https://doi.org/10.1029/2019WR026973.

Yao, W.L., Mostafa, S., Yang, Z., and Xu, G. 2020. Role of natural fractures characteristics on the performance of hydraulic fracturing for deep energy extraction using discrete fracture network (DFN). Eng Fract Mech 230, 106962. https://doi.org/10.1016/j.engfracmech.2020.106962.

Yao, Y.B., and Liu, D.M. 2012. Comparison of low-field NMR and mercury intrusion porosimetry in characterizing pore size distributions of coals. Fuel 95, 152–158. https://doi.org/10.1016/j.fuel.2011.12.039.

Yao, Y.B., Liu, D.M., Che, Y., Tang, D.Z., Tang, S.H., and Huang, W.H. 2009. Non-destructive characterization of coal samples from China using microfocus X-ray computed tomography. Int J Coal Geol 80(2), 113–123. https://doi.org/10.1016/j.coal.2009.08.001.

Yin, S., Jia, Q., and Ding, W.L. 2018. 3D paleotectonic stress field simulations and fracture prediction for marine-continental transitional facies forming a tight-sandstone reservoir in a highly deformed area. J Geophys Eng.15(5),1214-1230. https://doi.org/10.1088/1742-2140/aaad97.

Yuan, X.H., Yao, Y.B., Liu, D.M., and Pan, Z.J. 2019. Spontaneous imbibition in coal: Experimental and model analysis. J Nat Gas Sci Eng 67, 108–121. https://doi.org/10.1016/j.jngse.2019.04.016.

Zhai, C., Yu, X., Xiang, X.W., Li, Q.G., Wu, S.L., and Xu, J.Z. 2015. Experimental study of pulsating water pressure propagation in CBM reservoirs during pulse hydraulic fracturing. J Nat Gas Sci Eng 25, 15–22. https://doi.org/10.1016/j.jngse.2015.04.027.

Zhang, Xiaoyang, Wu, C., and Liu, S. 2017. Characteristic analysis and fractal model of the gas-water relative permeability of coal under different confining pressures. J Petrol Sci Eng 159, 488–496. https://doi.org/10.1016/j.petrol.2017.09.057.

Zhang, X.Y., Morrow, N. R., and Ma, S. 1996. Experimental verification of a modified scaling group for spontaneous imbibition. SPE Reservoir Engineering 11(04), 280–285. https://doi.org/10.2118/30762-PA.

Zhou, H. W., Zhong, J. C., Ren, W. G., Wang, X. Y., and Yi, H. Y. 2018. Characterization of pore-fracture networks and their evolution at various measurement scales in coal samples using X-ray μCT and a fractal method. Int J Coal Geol 189(November 2017), 35–49. https://doi.org/10.1016/j.coal.2018.02.007.

Zhou, S.D., Liu, D.M., Cai, Y.D., Yao, Y.B., and Li, Z.T.2017. 3D characterization and quantitative evaluation of pore-fracture networks of two Chinese coals using FIB-SEM tomography. Int J Coal Geol, 174, 41-54. https://doi.org/10.1016/j.coal.2017.03.008.

Zhou, T., Zhang, S.C., Yang, L., Ma, X.F., Zou, Y.S, and Lin, H. 2016. Experimental investigation on fracture surface strength softening induced by fracturing fluid imbibition and its impacts on flow conductivity in shale reservoirs. J Nat Gas Sci Eng 36, 893–905. https://doi.org/10.1016/j.jngse.2016.10.036.

Zhou, Z., Abass, H., Li, X., and Teklu, T. 2016. Experimental investigation of the effect of imbibition on shale permeability during hydraulic fracturing. J Nat Gas Sci Eng 29, 413-430. https://doi.org/10.1016/j.jngse.2016.01.023.

Zhu, W., Cai, X. N., Yang, L., Xia, J., Zhou, Y. C., and Pi, Z. P. 2019. The evolution of pores in thermal barrier coatings under volcanic ash corrosion using X-ray computed tomography. Surf Coat Tech 357, 372–378. https://doi.org/10.1016/j.surfcoat.2018.10.029.

Zolfaghari, A., Dehghanpour, H., and Holyk, J. 2017. Water sorption behaviour of gas shales: I. Role of clays. Int J Coal Geol 179, 130–138. https://doi.org/10.1016/j.coal.2017.05.008.

Captions for figures and tables

Fig.1 Water droplet on the surfaces of coal. (a) Contact angle of WD sample is 15°;(b) Contact angle of WZX sample is 67.5°. The smaller the contact angle, the stronger the hydrophilicity.

Fig.2 The schematic diagram of in situ dynamic spontaneous imbibition setup with X-ray μ-CT. The bottom part of the acrylic plastic tube was filled KI solution (10% weight) in this work. The coal plug was obtained parallel to the bedding with 2.5 cm in diameter.

Fig.3 The 520th CT slice images of the WD sample obtained by X-ray μ-CT. (a) dry condition; (b) spontaneous imbibition for 15 min; (c) the difference between (a) and (b); (d) the image was segmented for fracture using a segmentation method of Top-Hat segmentation; (e) the image was segmented for mineral by Top-Hat segmentation method; (f) the image was segmented for imbibition water by local thresholding method. (g) histogram showing relative fracture intensity, section line of Fig.3a (A-A'); (h) histogram showing relative mineral intensity in coal, section line of Fig.3a (B-B'); (i) histogram showing imbibition water relative intensity in coal, section line of Fig.3c (C-C').

Fig.4 The results of mercury intrusion porosimetry of WD and WZX. (a) The mercury intrusion/extrusion curves of WD; (b) pore size distribution of WD; (c) The calculation results of lg(r) versus lg(S) of WD based on Eq. (7), (d) The mercury intrusion/extrusion curves of WZX; (e) Pore size distribution of WZX, the slope of fitting line is 0.29; (f) The calculation results of lg(r) versus lg(S) of WZX, the slope of fitting line is 0.4.

Fig.5 Water distribution in sample WD at different times under spontaneous imbibition conditions. (a)-(f) spontaneous imbibition for 15 min,1h ,2h, 4h, 10h, 24h, respectively.

(g) difference between 2 h of water imbibition and dry condition; (h) difference between 24 h of water imbibition and dry condition for the WD sample.

Fig.6 The experimental results of water imbibition saturation versus imbibition time: (a)Sample WD, (b)Sample WZX. PI represents capillary zone, PII represents transition zone, PIII represents gravity zone.

Fig.7 Main imbibition pathway at different time. (a)the difference between micro-CT images after 15 min of imbibition and micro-CT images after 1 h of imbibition, main imbibition pathway is pore in matrix; (b)the difference between micro-CT images after 4 h of imbibition and micro-CT images after 10 h of imbibition, main imbibition pathways are pore in matrix and fracture; (c)the difference between micro-CT images after 10 h of imbibition and micro-CT images after 24 h of imbibition, main imbibition pathway is fracture.

Fig.8 2D pore-fracture morphology of the sample by SEM. (a) shows fracture and irregular pores of WD; (b) presents nano-pore and macropore structure of WD with small viewing angle; (b) shows "X" shear fractures of WZX, ①: fracture 1, ②: fracture 2; (c) exhibits intercrystallite pore and mineral distribution of WZX.

Fig.9 The relationship between fracture porosity and imbibition volume. (a)-(f) spontaneous imbibition for 15 min,1h ,2h, 4h, 10h, 24h, respectively.

Fig.10 Thin water film on the fracture surface. (a) imbibition for 10 hours, (b) imbibition for 24 hours.

Fig.11 The schematic of four stages during SI. Stage I: water was imbibed into pores and micro-fractures rapidly by capillary; Stage II: water was continue imbibed into lager fracture; Stage III: water imbibition exchange between micro-fractures and macro-fractures frequently; Stage IV: thin water film was formatted on the surface of macro-fractures. Fig.12 Water distribution under the SI. (a1) –(a6) water in different scale fracture by spontaneous imbibition for 15 min,1h ,2h, 4h, 10h, 24h, respectively; (b) the difference of water distribution between (a2) - (a1); (c) the difference of water distribution between (a3) - (a2); (d) the difference of water distribution between (a4) - (a3); (e) the difference of water distribution between (a5) - (a4); (f) the difference of water distribution between (a6) - (a5).

Fig.13 The relationship between mineral content and imbibition volume in sample WZX. Water imbibition volume increases with increasing mineral content in coal during the period of spontaneous imbibition.

Fig.14 The relationship between mineral content and imbibition volume in sample WZX. (a), (b)Gas-water relative permeability curves for WD sample and WZX sample, respectively;(c), (d) the relationship between gas-water permeability and imbibition time for WD sample and WZX sample, respectively.

Table 1 $R_{o,max}$, size, and proximate analysis and mineral content data of coal samples

Table 2 Spontaneous imbibition height and Spontaneous imbibition saturation of the selected coal samples at different time.

Table 3 Spontaneous imbibition stage and a corresponding main imbibition pathway of WD and WZX.

Table 4 The fitted equation and correlation coefficient between mineral content and imbibition volume at different time.

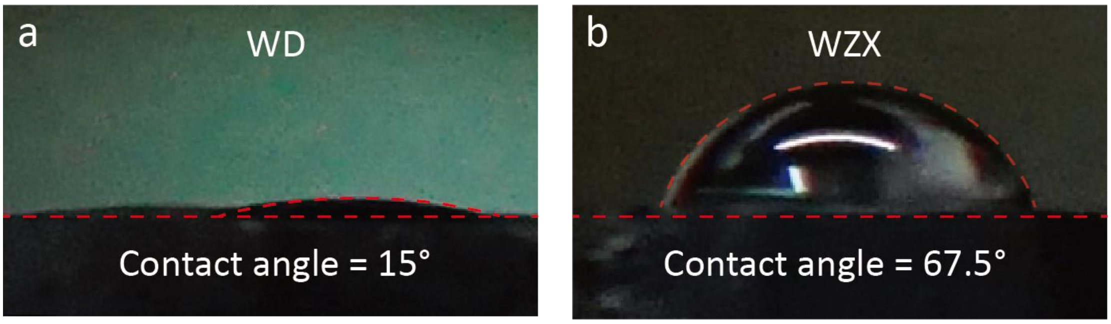

Fig.1

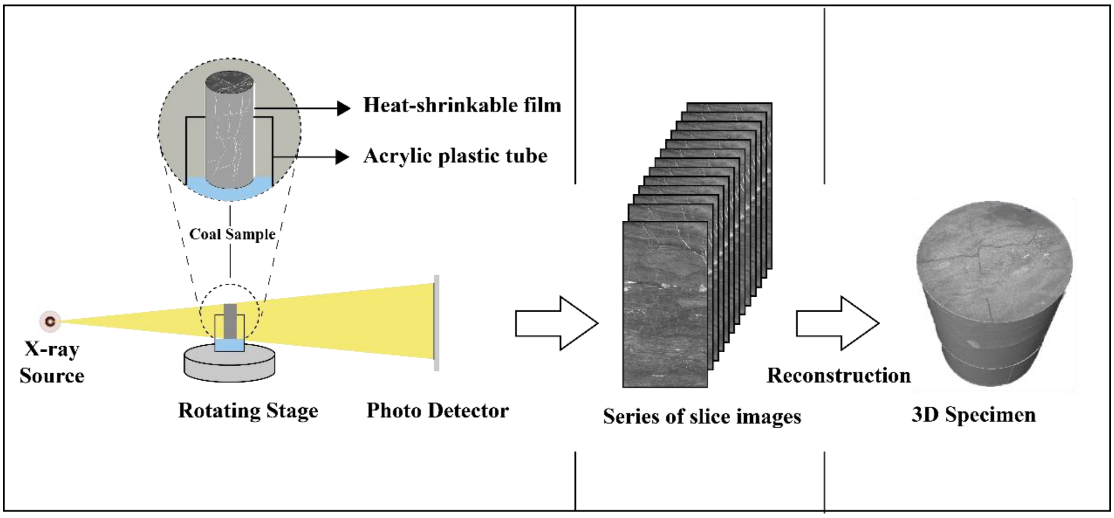
Heat-shrinkable film
Acrylic plastic tube
Coal Sample
X-ray
Source
Rotating Stage
Photo Detector
Series of slice images
Reconstruction
3D Specimen

Fig.2

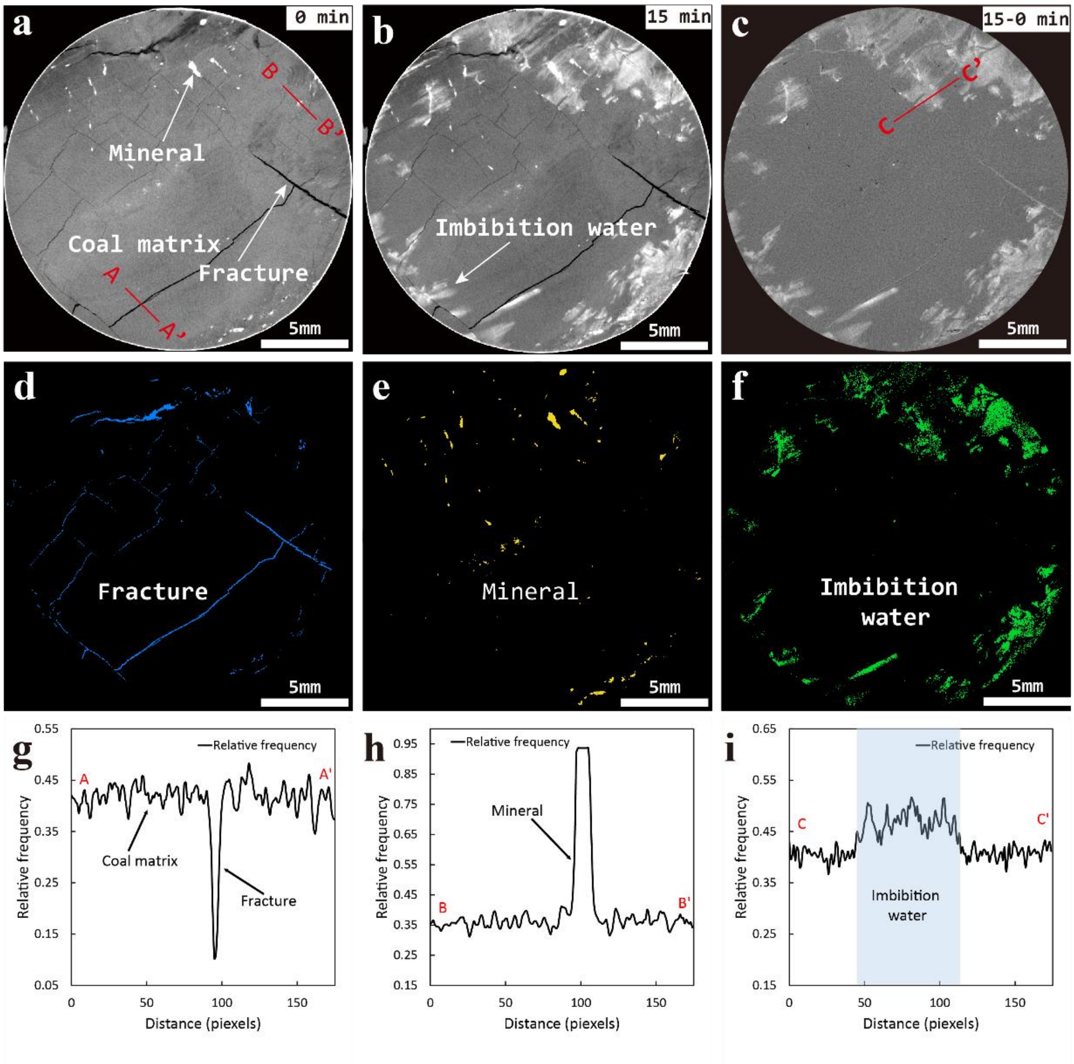
a
0 min
Mineral
Coal matrix
Fracture
B
B'
A
A'
5mm
b
15 min
Imbibition water
5mm
c
15-0 min
C
C'
5mm
d
Fracture
5mm
e
Mineral
5mm
f
Imbibition water
5mm
g
Relative frequency
A
A'
Coal matrix
Fracture
Relative frequency
Distance (piexels)
h
Relative frequency
Mineral
B
B'
Relative frequency
Distance (piexels)
i
Relative frequency
C
C'
Imbibition water
Relative frequency
Distance (piexels)

Fig.3

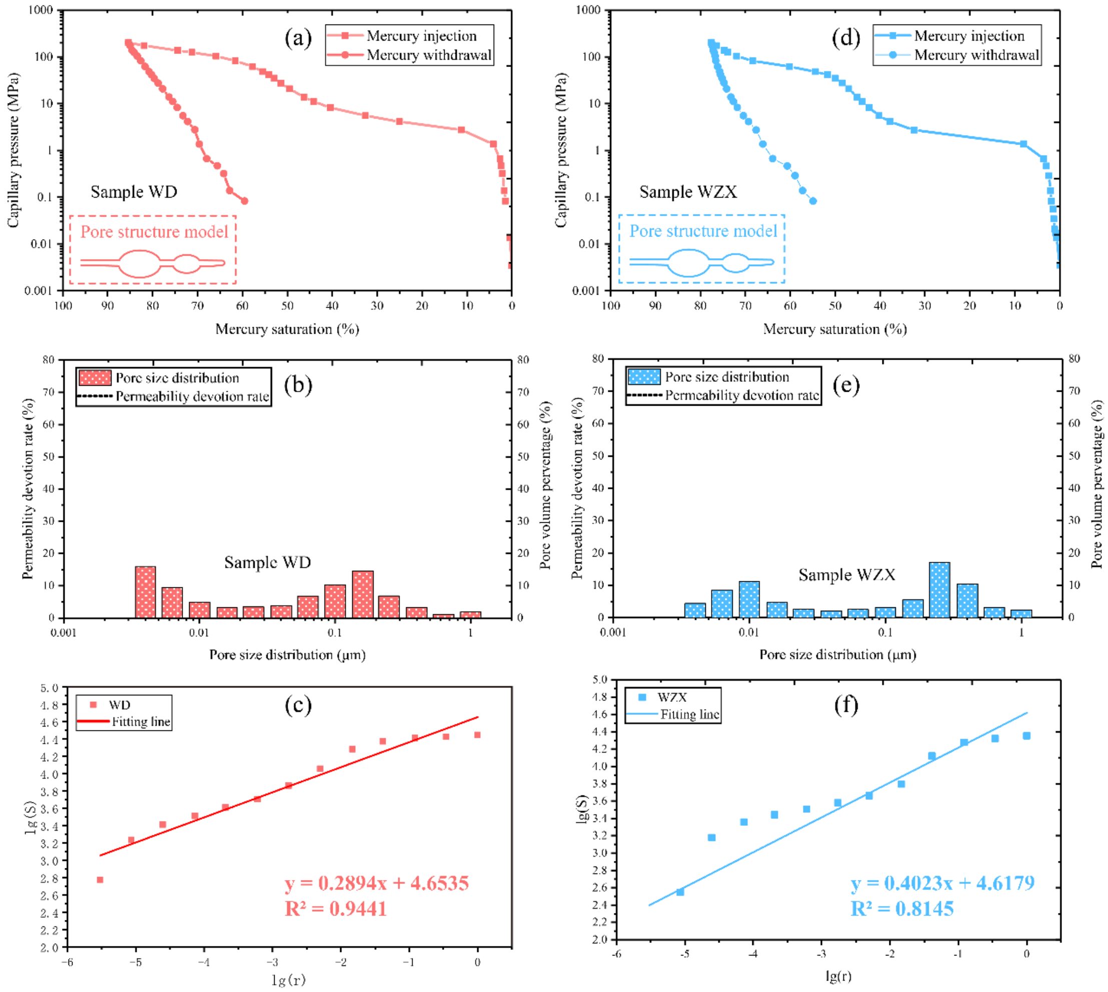

(a)
Mercury injection
Mercury withdrawal
Sample WD
Pore structure model
Capillary pressure (MPa)
Mercury saturation (%)
(d)
Mercury injection
Mercury withdrawal
Sample WZX
Pore structure model
Capillary pressure (MPa)
Mercury saturation (%)
(b)
Pore size distribution
Permeability devotion rate
Sample WD
Permeability devotion rate (%)
Pore volume perventage (%)
Pore size distribution (μm)
(e)
Pore size distribution
Permeability devotion rate
Sample WZX
Permeability devotion rate (%)
Pore volume perventage (%)
Pore size distribution (μm)
(c)
WD
Fitting line
y = 0.2894x + 4.6535
R² = 0.9441
lg(S)
lg(r)
(f)
WZX
Fitting line
y = 0.4023x + 4.6179
R² = 0.8145
lg(S)
lg(r)

Fig.4

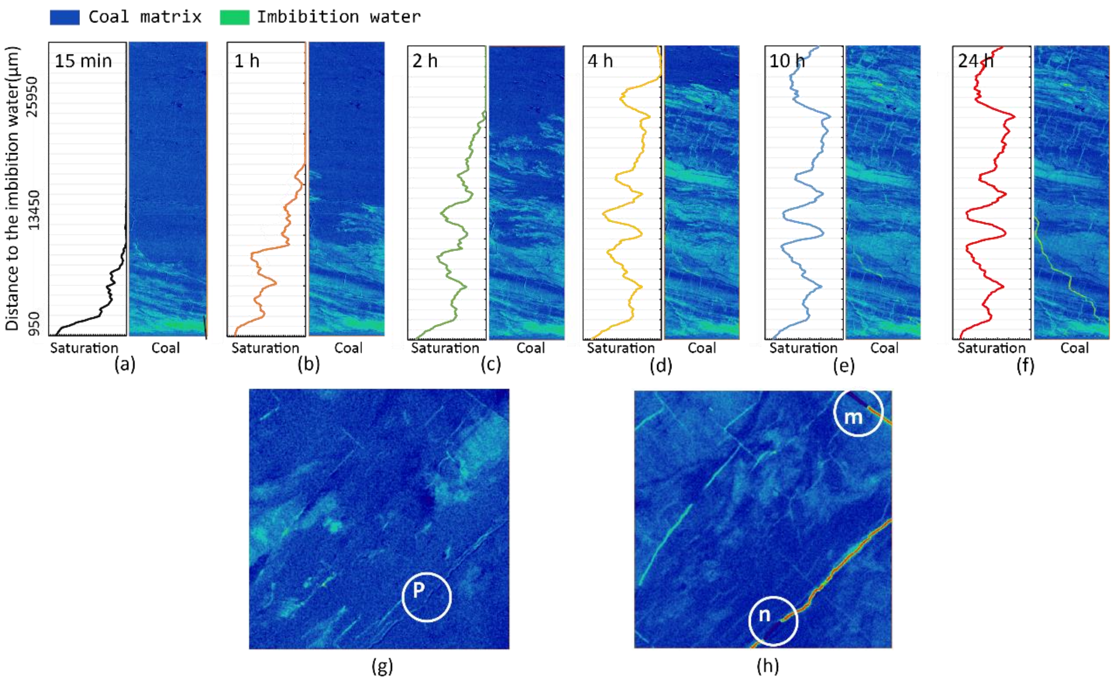
Coal matrix
Imbibition water
Distance to the imbibition water(μm)
25950
13450
950
15 min
1 h
2 h
4 h
10 h
24 h
Saturation
Coal
(a)
(b)
(c)
(d)
(e)
(f)
P
m
n
(g)
(h)

Fig.5

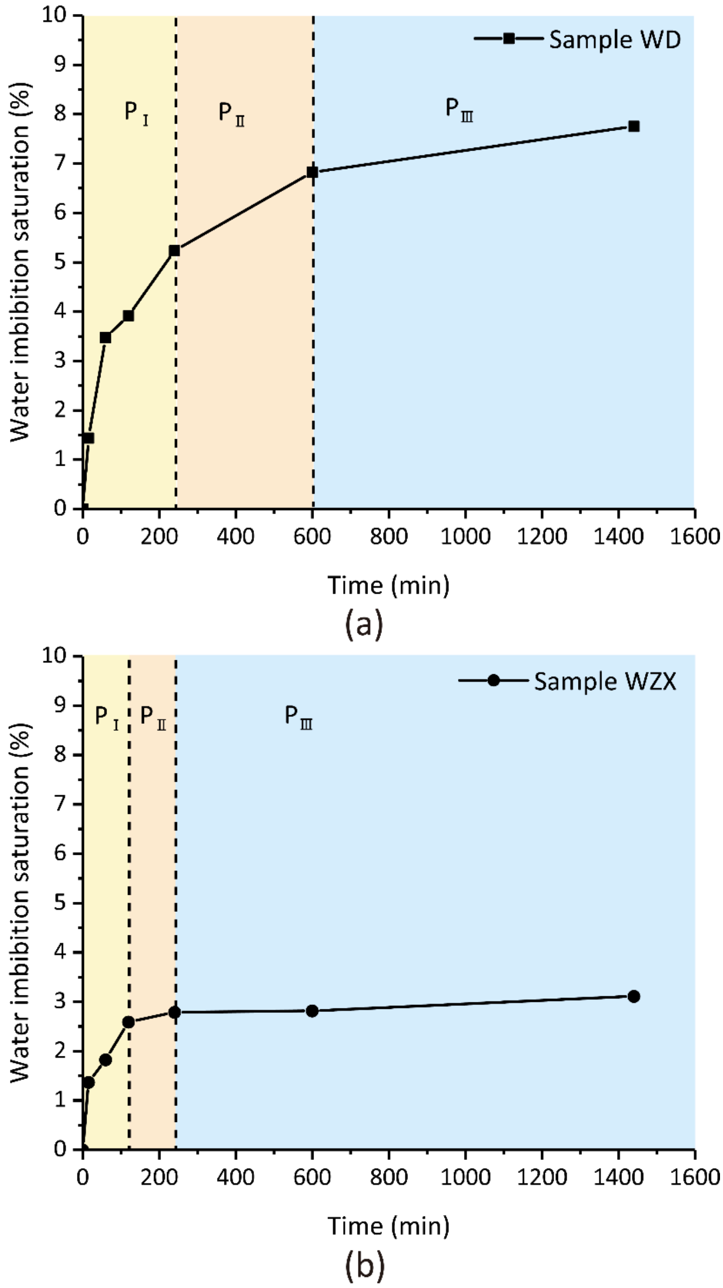
Sample WD
PⅠ
PⅡ
PⅢ
Water imbibition saturation (%)
Time (min)
(a)
Sample WZX
PⅠ
PⅡ
PⅢ
Water imbibition saturation (%)
Time (min)
(b)

Fig.6

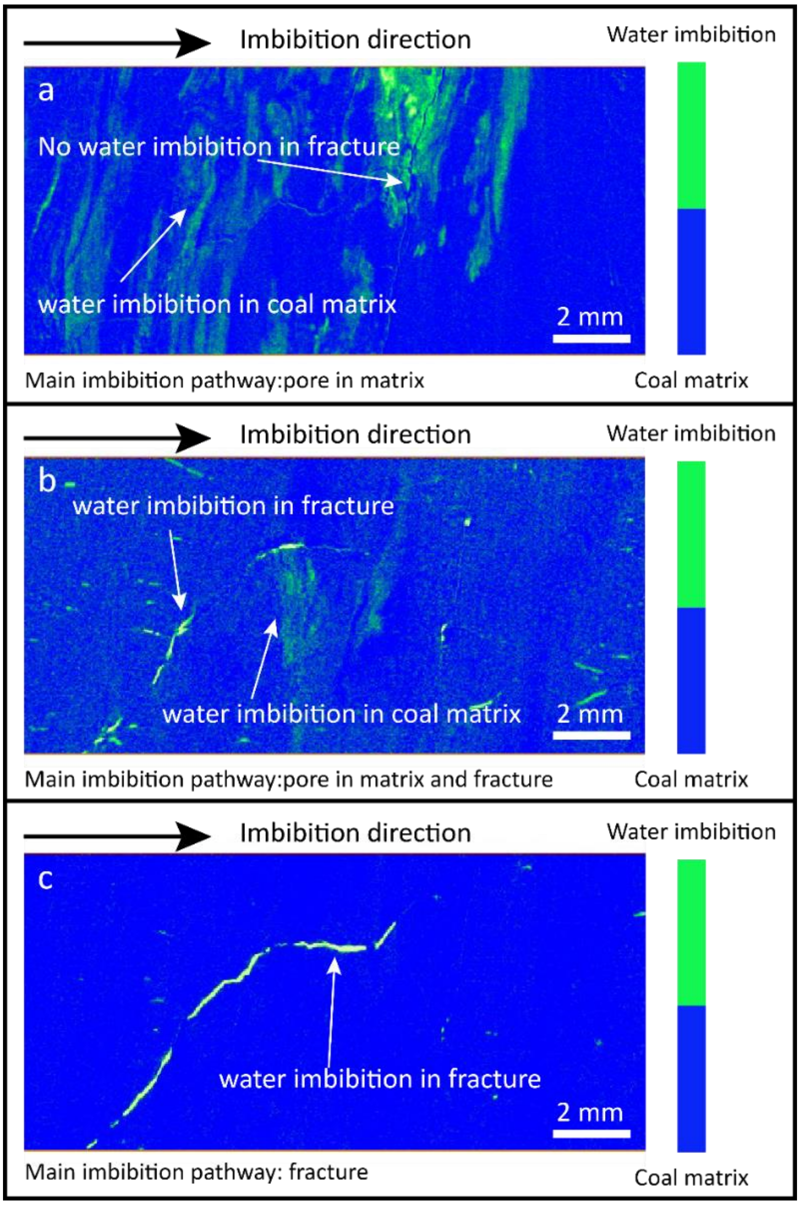
Imbibition direction
Water imbibition
a
No water imbibition in fracture
water imbibition in coal matrix
2 mm
Main imbibition pathway:pore in matrix
Coal matrix
Imbibition direction
Water imbibition
b
water imbibition in fracture
water imbibition in coal matrix
2 mm
Main imbibition pathway:pore in matrix and fracture
Coal matrix
Imbibition direction
Water imbibition
c
water imbibition in fracture
2 mm
Main imbibition pathway: fracture
Coal matrix

Fig.7

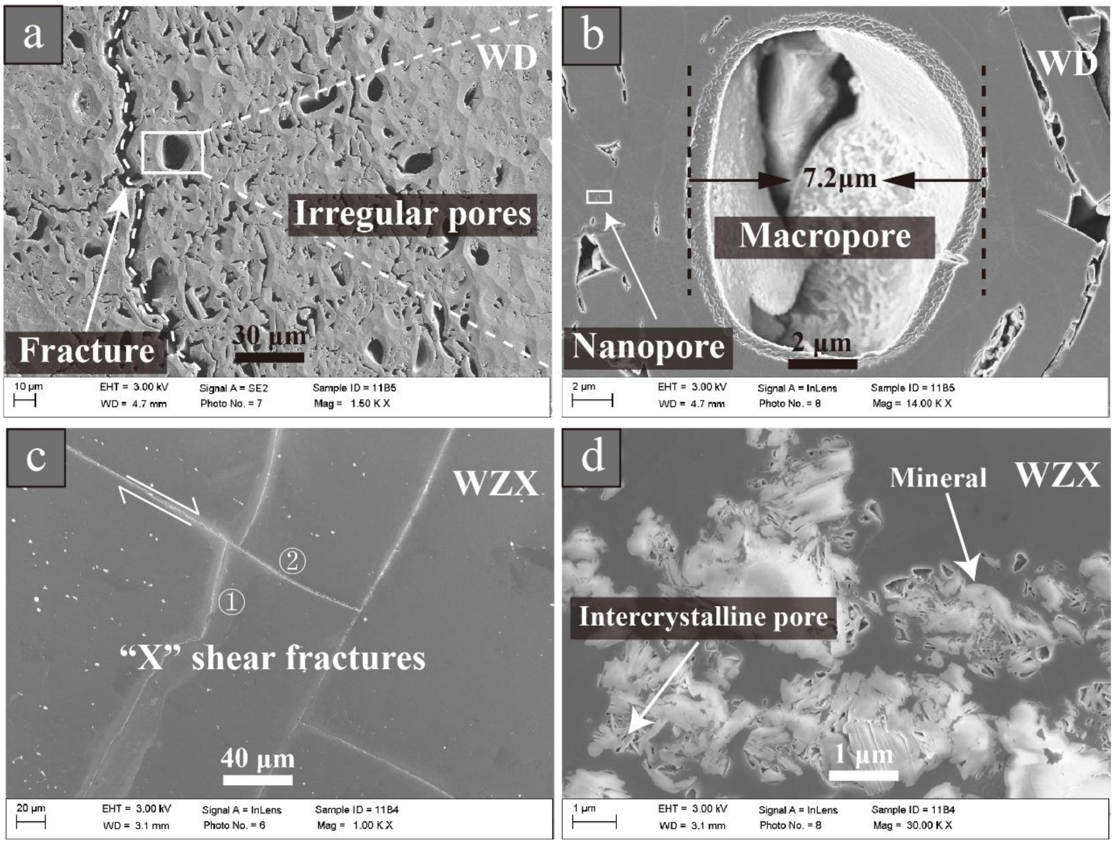

a
WD
Irregular pores
Fracture
30 μm
10 μm EHT = 3.00 kV Signal A = SE2 Sample ID = 11B5
WD = 4.7 mm Photo No. = 7 Mag = 1.50 K X
b
WD
7.2μm
Macropore
Nanopore
2 μm
2 μm EHT = 3.00 kV Signal A = InLens Sample ID = 11B5
WD = 4.7 mm Photo No. = 8 Mag = 14.00 K X
c
WZX
②
①
"X" shear fractures
40 μm
20 μm EHT = 3.00 kV Signal A = InLens Sample ID = 11B4
WD = 3.1 mm Photo No. = 6 Mag = 1.00 K X
d
Mineral
WZX
Intercrystalline pore
1 μm
1 μm EHT = 3.00 kV Signal A = InLens Sample ID = 11B4
WD = 3.1 mm Photo No. = 8 Mag = 30.00 K X

Fig.8

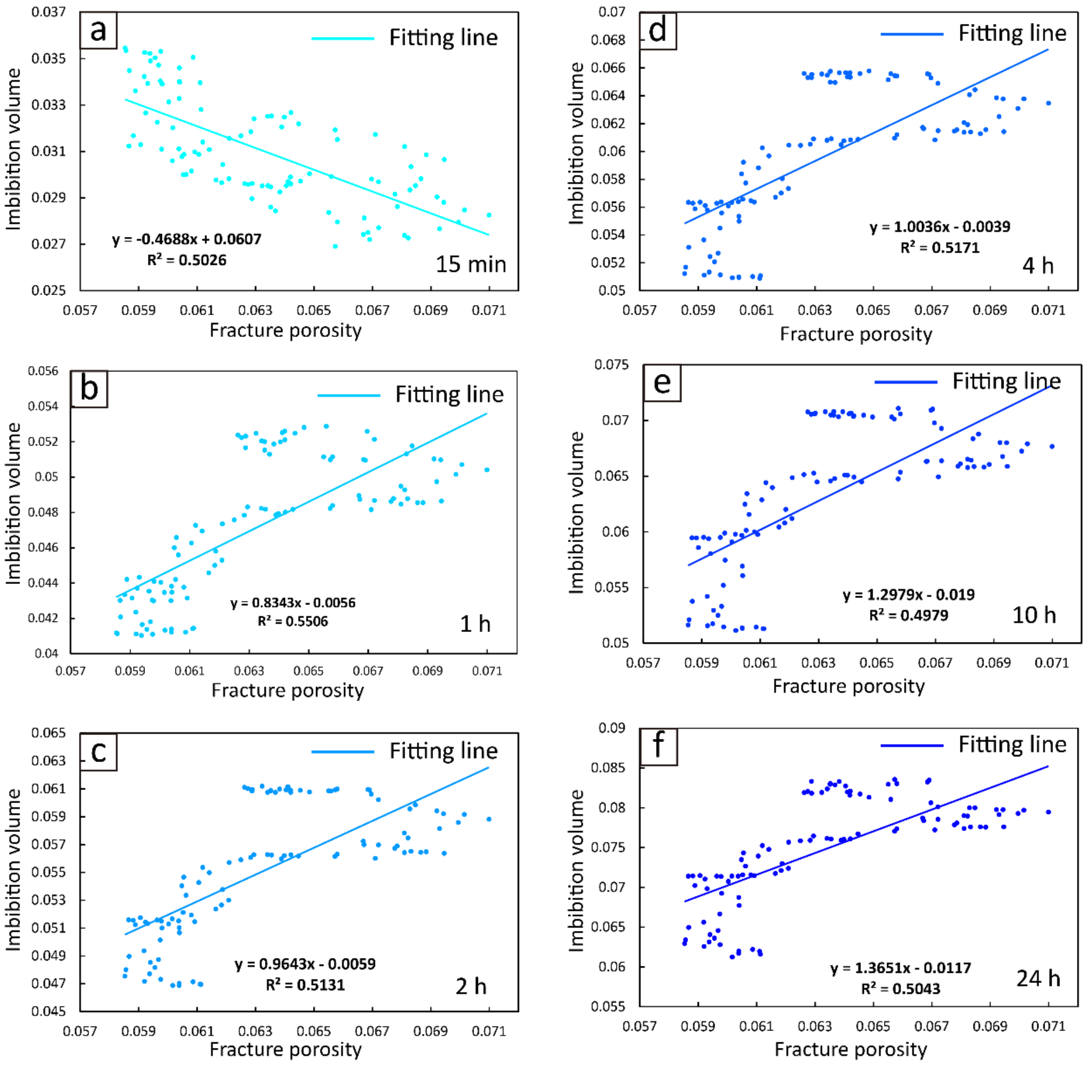
a
Fitting line
y = -0.4688x + 0.0607
R² = 0.5026
15 min
Imbibition volume
Fracture porosity
b
Fitting line
y = 0.8343x - 0.0056
R² = 0.5506
1 h
Imbibition volume
Fracture porosity
c
Fitting line
y = 0.9643x - 0.0059
R² = 0.5131
2 h
Imbibition volume
Fracture porosity
d
Fitting line
y = 1.0036x - 0.0039
R² = 0.5171
4 h
Imbibition volume
Fracture porosity
e
Fitting line
y = 1.2979x - 0.019
R² = 0.4979
10 h
Imbibition volume
Fracture porosity
f
Fitting line
y = 1.3651x - 0.0117
R² = 0.5043
24 h
Imbibition volume
Fracture porosity

Fig.9

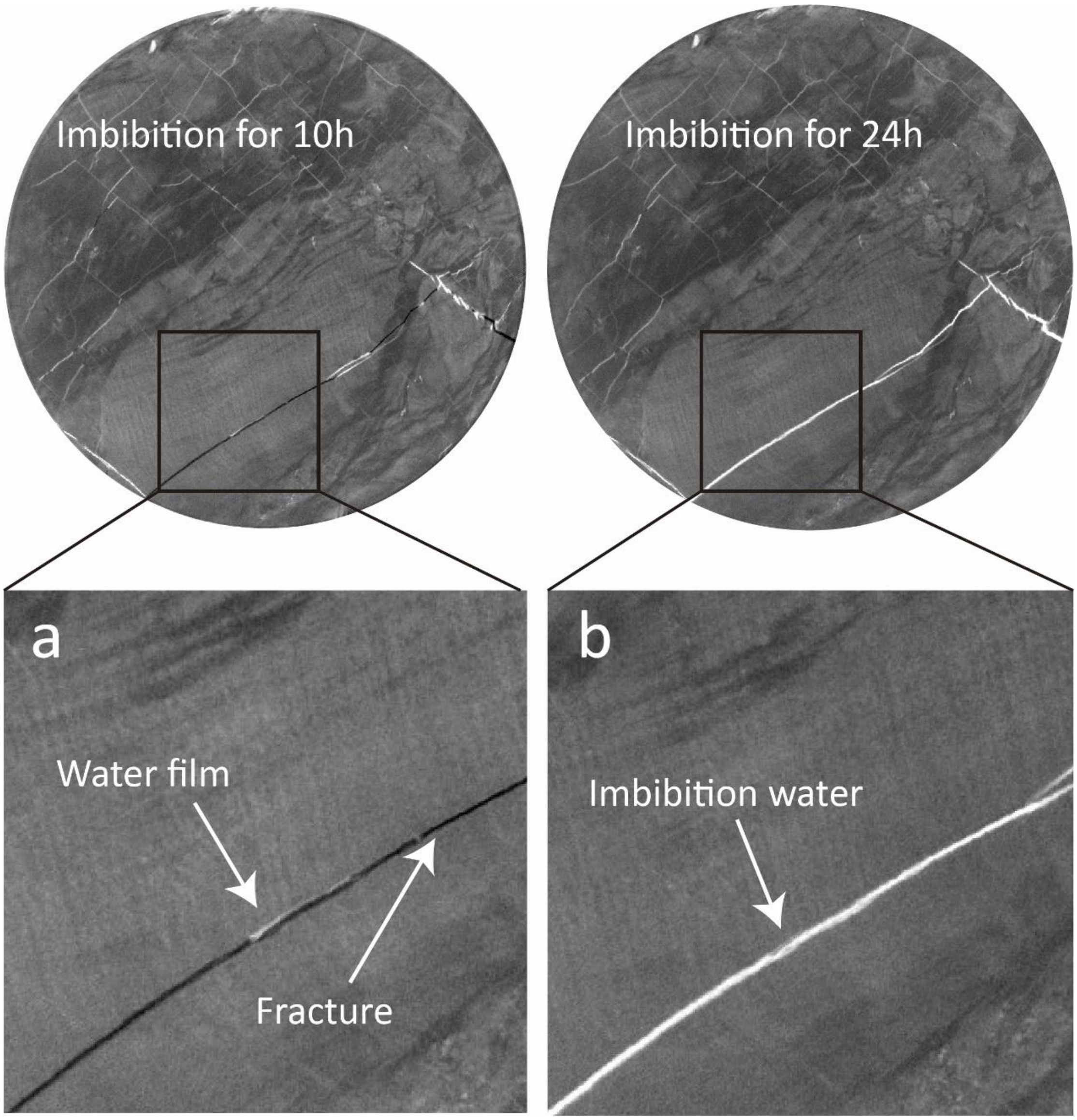
Imbibition for 10h
Imbibition for 24h
a
Water film
Fracture
b
Imbibition water

Fig.10

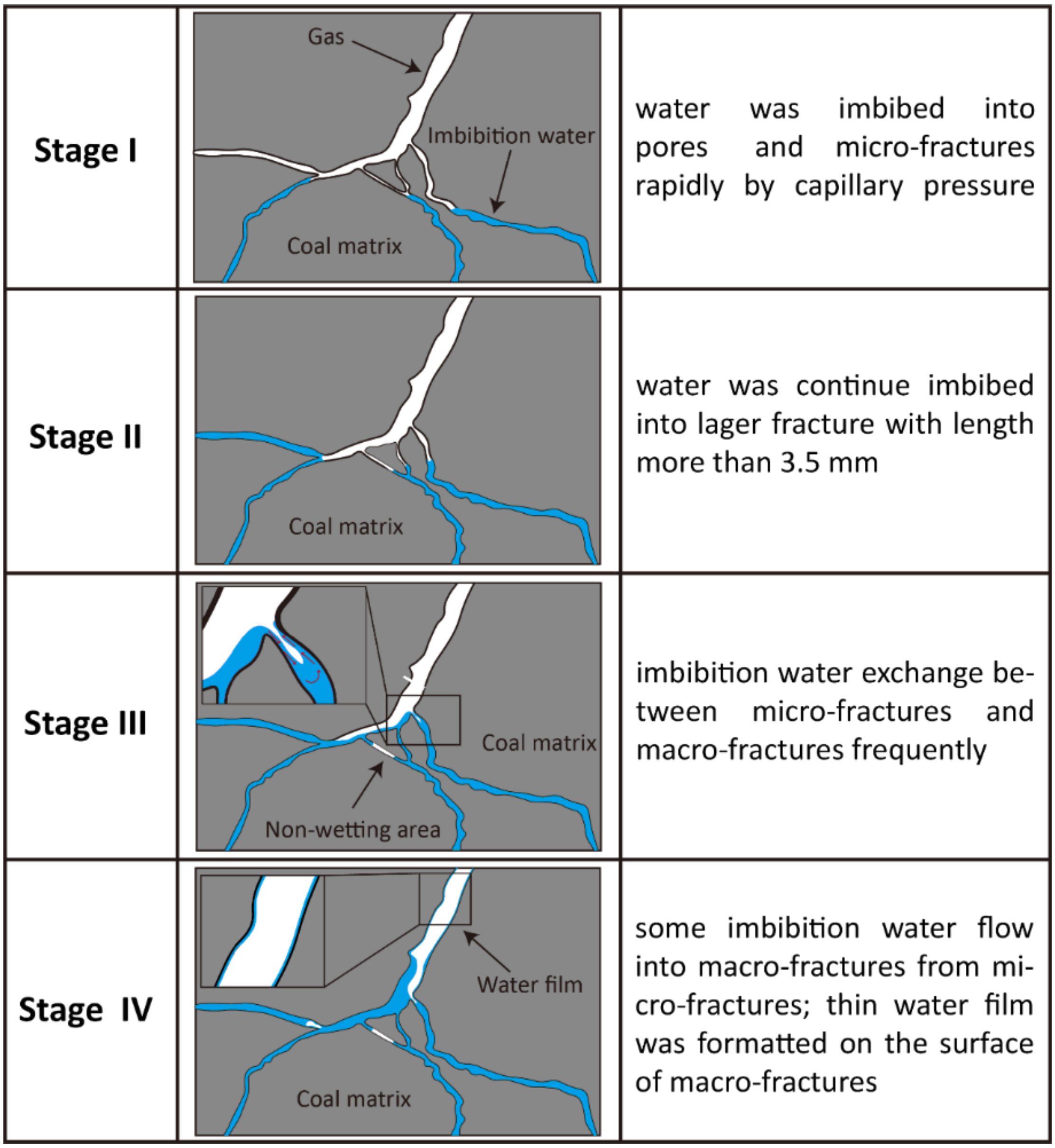
Stage I
Gas
Imbibition water
Coal matrix
water was imbibed into pores and micro-fractures rapidly by capillary pressure
Stage II
Coal matrix
water was continue imbibed into lager fracture with length more than 3.5 mm
Stage III
Coal matrix
Non-wetting area
imbibition water exchange be-tween micro-fractures and macro-fractures frequently
Stage IV
Water film
Coal matrix
some imbibition water flow into macro-fractures from mi-cro-fractures; thin water film was formatted on the surface of macro-fractures

Fig.11

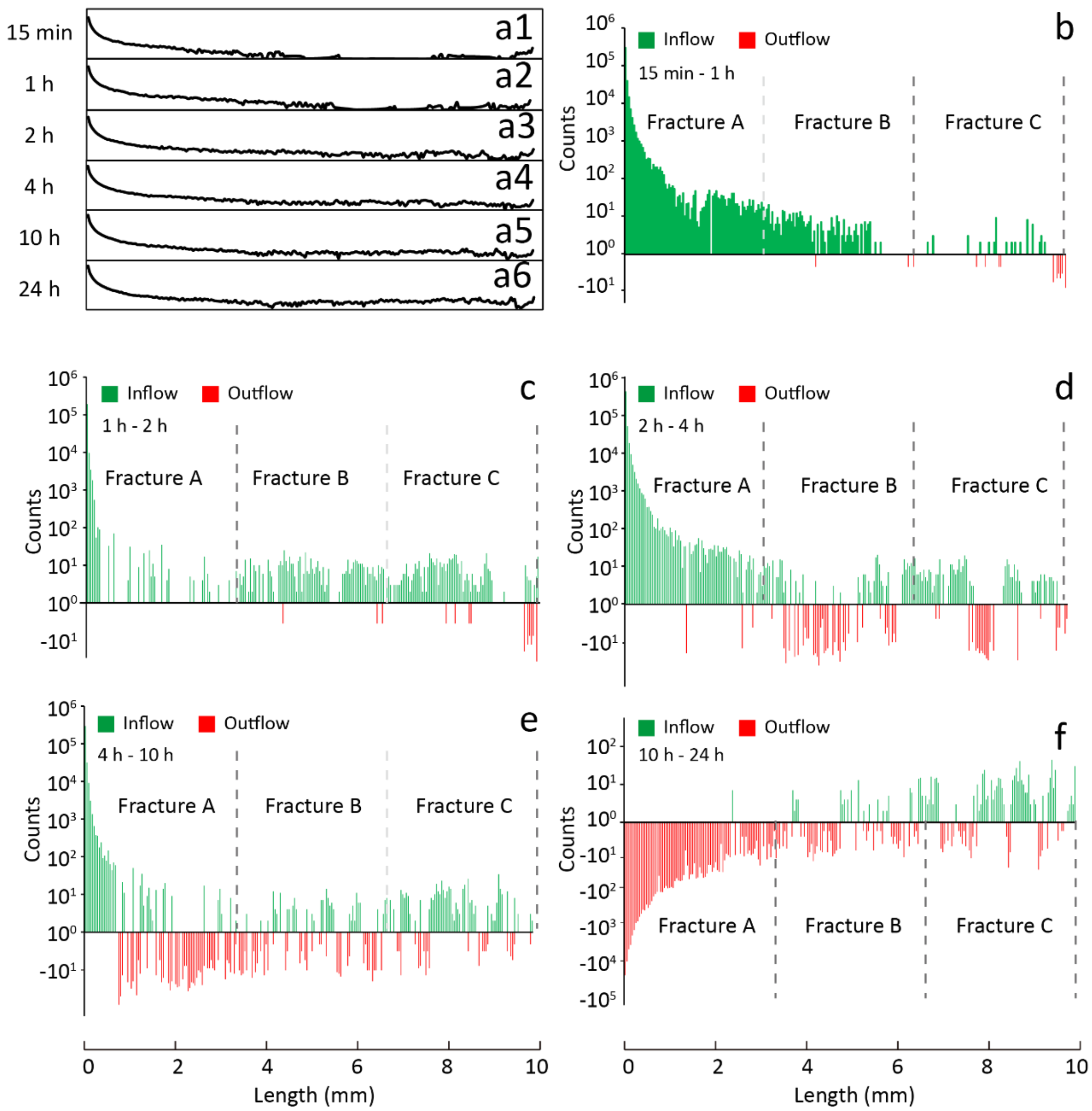
15 min
1 h
2 h
4 h
10 h
24 h
a1
a2
a3
a4
a5
a6
b
Inflow
Outflow
15 min - 1 h
Fracture A
Fracture B
Fracture C
Counts
c
1 h - 2 h
d
2 h - 4 h
e
4 h - 10 h
f
10 h - 24 h
Length (mm)

Fig.12

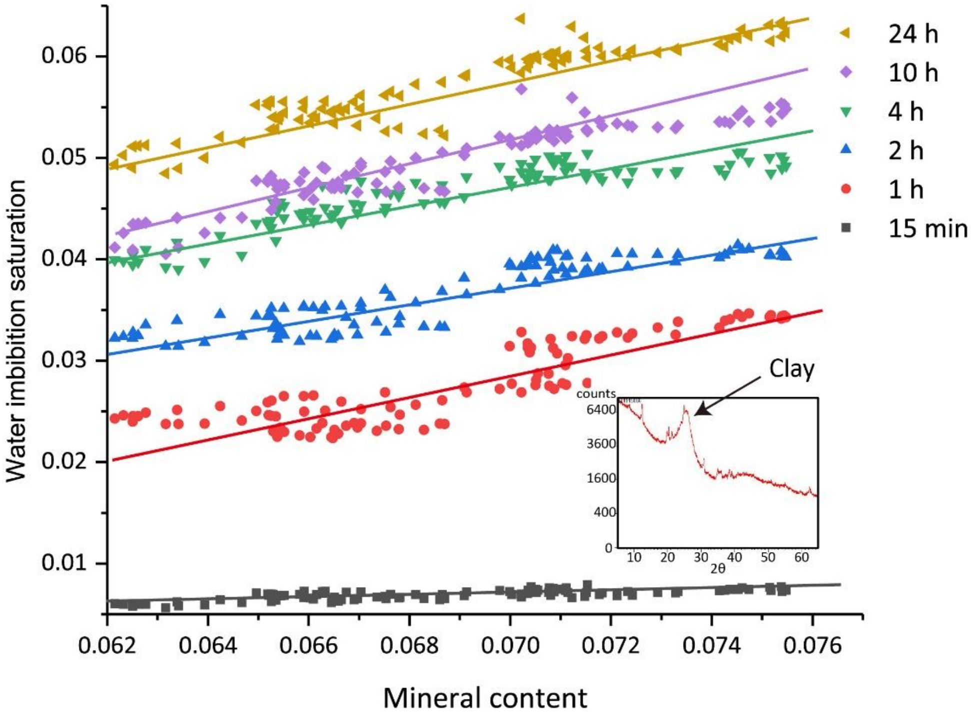
Water imbibition saturation
Mineral content
24 h
10 h
4 h
2 h
1 h
15 min
Clay
counts
2θ

Fig.13

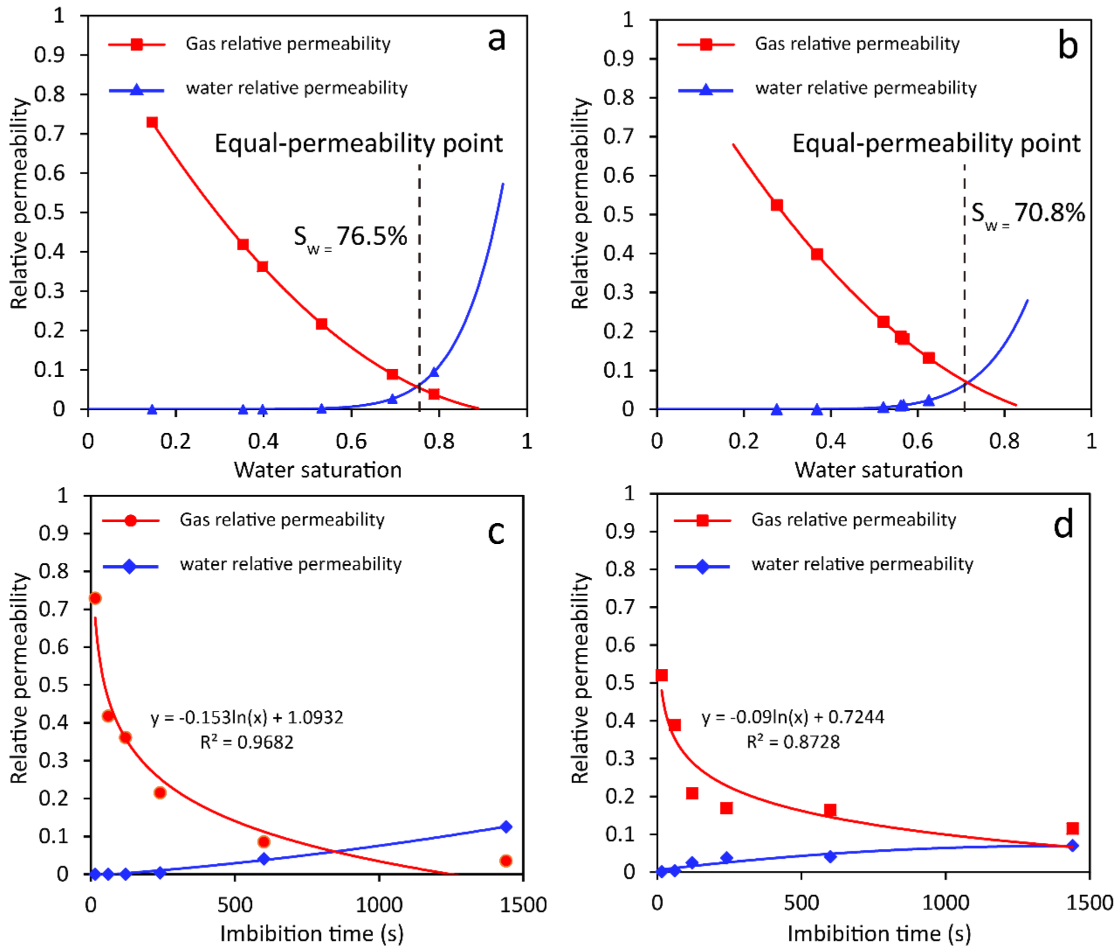

a
Gas relative permeability
water relative permeability
Equal-permeability point
Sw = 76.5%
Relative permeability
Water saturation
b
Gas relative permeability
water relative permeability
Equal-permeability point
Sw = 70.8%
Relative permeability
Water saturation
c
Gas relative permeability
water relative permeability
y = -0.153ln(x) + 1.0932
R² = 0.9682
Relative permeability
Imbibition time (s)
d
Gas relative permeability
water relative permeability
y = -0.09ln(x) + 0.7244
R² = 0.8728
Relative permeability
Imbibition time (s)

Fig.14

Table 1 $R_{o,max}$, porpsity, permeability, proximate analysis and mineral content data of coal samples

Sample	$R_{o, max}$	Porosity	Perm.	Proximate analysis (%)				Mineral content (%)					
	(%)	(%)	(md)	M_{ad}	A_{ad}	V_{ad}	FC_{ad}	*Q*	*Ca*	*Do*	*Si*	*Py*	*Clay*
WD	0.68	9.84	1.21	2.18	1.45	67.28	29.09	0	0	0	0	0	100
WZX	2.05	4.97	0.1014	1.17	7.85	82.35	8.63	0	0	11	0	0	89

Note: $R_{o, max}$-maximum vitrinite reflectance; L-Length; D-Diameter; Perm-Permeability. - M_{ad}-moisture (air-dried basis); A_{ad}-ash content (airdried basis); V_{ad}-volatile content (air-dried basis); FC_{ad}-fixed carbon (air-dried basis); *Q*-Quartz; *Ca*-Calcite; *Do*-Dolomite; *Si*-Siderite; *Py*-Pyrite;

Table 2 Spontaneous imbibition height and Spontaneous imbibition saturation of the selected coal samples at different time

Imbibition time	Sample WD.		Sample WZX	
	SIH	SIS	SIH	SIS
15min	29.23%	1.44%	88.32%	1.37%
1h	57.42%	3.47%	100%	1.83%
2h	76.69%	3.92%	100%	2.57%
4h	89.49%	5.24%	100%	2.79%
10h	100%	6.82%	100%	2.82%
24h	100%	7.76%	100%	3.11%

Note: SIH-Spontaneous imbibition height; SIS- Spontaneous imbibition saturation.

Table 3 Spontaneous imbibition stage and a corresponding main imbibition pathway of WD and WZX

Imbibition stage	Imbibition time (min)		Main imbibition pathway
	Sample WD	Sample WZX	
capillary stage	0-240	0-120	pores in coal matrix
transition stage	240-600	120-240	pores and micro-fractures
gravity stage	>600	>240	fractures

Table 4 The fitted equation and correlation coefficient between mineral content and imbibition volume at different time

Imbibition time	Fitted equation	Correlation coefficient
15 min	y = 0.1038x - 0.0002	0.5701
1 h	y = 0.9742x - 0.0394	0.7735
2 h	y = 0.8061x - 0.0189	0.8065
4 h	y = 0.7584x - 0.0058	0.801
10 h	y = 0.9668x - 0.0169	0.8752
24 h	y = 1.0035x - 0.0121	0.8707